Journal of Power Sources 257 (2014) 308–318

Contents lists available at ScienceDirect

Journal of Power Sources

journal homepage: www.elsevier.com/locate/jpowsour

Significant performance enhancement of yttrium-doped barium cerate proton conductor as electrolyte for solid oxide fuel cells through a Pd ingress–egress approach

Yu Liu [a], Ran Ran [a], Sidian Li [c], Yong Jiao [c], Moses O. Tade [b], Zongping Shao [a,b,*]

[a] State Key Laboratory of Materials-Oriented Chemical Engineering, Nanjing University of Technology, No. 5 Xin Mofan Road, Nanjing 210009, China
[b] Department of Chemical Engineering, Curtin University, Perth, WA 6845, Australia
[c] Institute of Molecular Science, Shanxi University, Taiyuan 030006, China

HIGHLIGHTS

- Enhancing the performance of BCY through a Pd ingress–egress approach.
- The introduction of Pd significantly improve sinterability.
- Pd egress from the BCYP10 perovskite lattice after reduction or calcination.
- A single cell with a BCYP10 electrolyte reaches a peak power density of 645 mA cm^{-2} at 700 °C.

ARTICLE INFO

Article history:
Received 10 December 2013
Received in revised form
22 January 2014
Accepted 4 February 2014
Available online 13 February 2014

Keywords:
Ingress and egress
Palladium
Proton conductor
Solid oxide fuel cell

ABSTRACT

Proton-conducting perovskite oxides are excellent electrolyte materials for SOFCs that may improve power density at reduced temperatures and increase fuel efficiency, thus encouraging the widespread implementation of this attractive technology. The main challenges in the application of these oxides in SOFCs are difficult sintering and insufficient conductivity in real cells. In this study, we propose a novel method to significantly enhance the performance of a yttrium-doped barium cerate proton conductor as an electrolyte for SOFCs through a Pd ingress–egress approach to the development of $BaCe_{0.8}Y_{0.1}Pd_{0.1}O_{3-\delta}$ (BCYP10). The capability of the Pd egress from the BCYP10 perovskite lattice is demonstrated by H_2-TPR, XRD, EDX mapping of STEM and XPS. Significant improvement in the sinterability is observed after the introduction of Pd due to the increased ionic conductivity and the sintering aid effect of egressed Pd. The formation of a B-site cation defect structure after Pd egress and the consequent modification of perovskite grain boundaries with Pd nanoparticles leads to a proton conductivity of BCYP10 that is approximately 3 times higher than that of BCY under a reducing atmosphere. A single cell with a thin film BCYP10 electrolyte reaches a peak power density as high as 645 mA cm^{-2} at 700 °C.

© 2014 Elsevier B.V. All rights reserved.

1. Introduction

Some oxides are conductive for specific ions, such as H^+, O^{2-}, Li^+ and Na^+ [1–4], and have found potential applications in a wide range of fields, from energy storage (all solid lithium-ion batteries) and energy conversion (electrolyzers and fuel cells) to sensing (electrochemical gas sensors) and catalysis (active catalyst supports) [5–10]. With the increasing demand for efficient and environmentally friendly energy systems, the direct conversion of gaseous fuels into electricity by fuel cells has received tremendous attention during the past decades [11,12]. Among these fuel cells, high-temperature solid oxide fuel cells (SOFCs), which are constructed from oxide-based solid ionic conductors, have been of particular interest for their fuel flexibility, high efficiency and high quality of exhaust heat [13–18].

Conventional SOFCs are composed of an oxygen ion conducting electrolyte, such as doped ceria and stabilized zirconia [19,20], which typically contain oxygen vacancies in their lattices as oxygen-ion carriers, created by the doping strategy. However, oxygen ions have a low mobility and a high activation enthalpy due to their

* Corresponding author. State Key Laboratory of Materials-Oriented Chemical Engineering, Nanjing University of Technology, No. 5 Xin Mofan Road, Nanjing 210009, China. Tel.: +86 25 83172256; fax: +86 25 83172242.
E-mail addresses: shaozp@yeah.net, shaozp@njut.edu.cn (Z. Shao).

http://dx.doi.org/10.1016/j.jpowsour.2014.02.013
0378-7753/© 2014 Elsevier B.V. All rights reserved.

large ionic size, making it difficult to achieve high oxygen ion conductivity at reduced temperatures. Compared to the oxygen ion (O^{2-}), a proton (H^+) has a much higher mobility because of its much smaller ionic size; it is thus easier to achieve a higher conductivity. At the beginning of the 1980s, Iwahara et al. first reported that some perovskite-type oxides possessed a high proton conductivity under a humidified atmosphere at intermediate temperatures [21]. Since that report, there has been tremendous interest in such materials, ranging from fundamental research to potential applications. In particular, proton-conducting SOFCs have attracted considerable attention during the last five years, and this research was stimulated by the SOFCs' great potential for reducing operation temperatures and increasing fuel efficiency by avoiding the dilution effect of the oxidation product to the fuel gas [22–25].

The proton conductivity of perovskite oxides is due to the presence of cationic defects in their lattice, created by the dissociated absorption of water with the presence of oxygen vacancies [26,27]. In Kröger–Vink notation, such a reaction is given as

$$H_2O + V_O^{\bullet\bullet} + O_O^x \rightarrow 2(OH)_O^{\bullet} \quad (1)$$

The hopping of a proton between adjacent oxygen sites is the origin of proton conductivity.

As an electrolyte of proton-conducting SOFCs, both high proton conductivity and facile densification are required. Perovskite materials based on $BaCeO_3$ and $BaZrO_3$ parent oxides are the most commonly investigated proton-conducting oxides; [28–32] in particular, doped $BaCeO_3$ shows the highest proton conductivity compared to the others [33]. However, the majority of proton-conducting SOFCs still showed a much lower power density compared to oxygen ion conducting SOFCs at reduced temperature [34,35]; in addition to the lack of a high-performance cathode, the relatively low conductivity of the electrolyte is an important factor. The proton conductivity of perovskite oxides is strongly affected by the dopant, sintering, grain boundary properties, and cation stoichiometry. Sometimes, the introduction of a well-dispersed second phase can significantly alter the macroscopic transport properties of the ionic conductors [34–36]. For example, O'Hayre et al. recently demonstrated an ionic composite of yttrium-doped barium zirconate (BYZ) and ~2 wt% Pd particles with a conductivity 1.5–2.7 times higher than that of pure BYZ; they further demonstrated that nanosized Pd as the metal phase was more effective than other sizes in improving the conductivity of BZY, likely due to the increased Pd–BZY grain boundary area. [37] Poor sintering is another important drawback of perovskite-type proton conductors that limits their practical use in SOFCs. For fuel cells in the anode-supported thin film electrolyte configuration, the constricted sintering sometimes makes it more difficult to achieve a dense electrolyte. Increasing the sintering temperature is a general way to achieve a better densification of ceramics; however, it may also lead to the over sintering of the anode substrate, a loss of barium because of evaporation, and increased energy consumption. Nanosizing the starting powder through advanced synthesis has also been widely attempted to improve the sintering of ceramics; however, doing so greatly increases the complexity of the fabrication process. Applying a sintering aid turned out to be a more effective way of increasing the sintering capability and reducing the sintering temperature for many ceramics.

Recently, it was found that some perovskite oxides can accommodate and release precious metal elements under controlled conditions [38–42]. Nishihata et al. were the first to present such a concept; they developed Pd-incorporated perovskites as self-regenerating or "intelligent" catalysts for automobile exhaust treatment [38]. In these catalysts, noble metals in their ionic state were incorporated into a perovskite host as nanosized metal particles decorating the perovskite surface, acting as the active catalyst under reducing conditions. Once the metal particles were sintered, they could be re-absorbed by the perovskite lattice under an oxidizing atmosphere. Previously, the oxide hosts were mainly based on $LaFeO_3$ or $La(Co,Fe)O_3$ perovskites [39,41]. The solubility of the precious metal element in these perovskite lattices is, however, relatively low. Recently, Rappe et al. demonstrated that the redox-controlled ingress and egress of palladium in a $BaCeO_3$ perovskite was also possible and that the Pd doping could reach nearly 10% of the B-site cation [42].

In this study, we report a novel method to improve the electrical conductivity and sintering of yttrium-doped $BaCeO_3$ perovskite oxide by utilizing the ingress and egress properties of palladium in the oxide lattice with the development of a $BaCe_{0.8}Y_{0.1}Pd_{0.1}O_{3-\delta}$ (BCYP10) perovskite. The presence of Pd^{2+} in the oxide lattice promoted the oxygen mobility and thus facilitated the membrane sintering at the earlier sintering stage, while Pd moved out of the perovskite lattice and performed as a sintering aid at higher sintering temperatures to result in the formation of a nano ionic composite made of a B-site cation-deficient perovskite and Pd nanoparticles with significantly improved conductivity. BCYP10 was finally applied as the electrolyte in a real fuel cell to achieve a high open circuit voltage (OCV) and power density at reduced temperature.

2. Experimental materials and methods

2.1. Materials synthesis

A complexing sol–gel process was used for the synthesis of $BaCe_{0.8}Y_{0.1}Pd_{0.1}O_{3-\delta}$ (BCYP10), where Pd was doped into the B site. In a typical synthesis, stoichiometric amounts of $Ba(NO_3)_2$, $Ce(NO_3)_3\cdot 6H_2O$, $Y(NO_3)_3\cdot 6H_2O$ and $Pd(NO_3)_2\cdot 2H_2O$ were first prepared as a mixed solution, then a proper amount of EDTA and citric acid were added to serve as the complexing agents. To prevent hydrolysis, $Pd(NO_3)_2\cdot 2H_2O$ was pre-dissolved in dilute nitric acid before use. The molar ratio of total metal ions to EDTA and citric acid was set at 1:1:2, and the pH of the solution was adjusted to approximately 6 by using aqueous ammonia. The mixed solution was then heated at 90 °C to evaporate the water, resulting in a transparent gel, which was then pretreated at 240 °C in an electrical oven to initiate the primary decomposition. Afterward, the resulting solid precursor was fired at 1000 °C in air at a heating rate of 5 °C min^{-1} to obtain the final product. A similar method was also used for the synthesis of $BaCe_{0.9}Y_{0.1}O_{3-\delta}$ (BCY), $BaCe_{0.8}Y_{0.1}O_{3-\delta}$ (BCY-non) and $Ba_{0.5}Sr_{0.5}Co_{0.8}Fe_{0.2}O_{3-\delta}$ (BSCF).

2.2. Cell fabrication

To fabricate the anode substrate, the as-prepared BCYP10 powder and commercial NiO (Chengdu Shudu Nano-Science Co., Ltd.) were mixed at a weight ratio of 40:60 by high energy ball milling in ethanol liquid medium (Fritsch, Pulverisette 6); polyvinyl butyral (PVB) was also introduced to the mixture as a pore-forming agent with a weight ratio of anode powders to PVB of 95:5. After ball milling at 400 rpm for 30 min, the obtained slurry was dried in an electric oven and formed into disc-shaped anode substrates by dry pressing under a hydraulic pressure of 150 MPa using a stainless steel die. Subsequently, the BCYP10 powders were added to the surface of the green disc-shaped anode substrates. The anode-electrolyte bi-layer cells were uniaxially co-pressed at 300 MPa and then sintered at 1400 °C for 5 h. The BSCF powder was mixed with glycerol, ethylene glycol and isopropyl alcohol via high-energy ball milling (Fritsch, Pulverisette 6) at 400 rpm for 40 min to form a colloidal suspension, which was painted onto the BCYP electrolyte

surface and then co-fired at 1000 °C for 2 h in air to act as the cathode of the cells. The coin-shaped cathode was approximately 20 μm thick and had an effective area of 0.48 cm^2. To prepare the BCYP10 electrolyte substrates for symmetrical cells, the appropriate amount of BCYP10 powders were pressed in a stainless steel die with a diameter of 15 mm at 300 MPa for 1 min. The green electrolyte substrates were then sintered at 1400 °C for 5 h at a heating rate of 5 °C min^{-1} to allow the densification of the electrolyte layers. For both the symmetrical cells and the dual-layer cells, silver paste and silver wires were adopted as the current collector and current leads, respectively.

2.3. Electrochemical characterization

Impedance spectra of the cells at OCV conditions were acquired using a frequency impedance analyzer (Solartron 1260) at temperatures ranging from 200 to 750 °C in wet air or wet 10%H_2–Ar atmospheres. The amplitude of the AC signal was 10 mV, and the frequency ranged from 0.1 Hz to 10^7 kHz. Zview was used to analyze the impedance data to obtain the bulk and grain boundary conductivities. The performance of an anode-supported single cell was tested in a home-constructed cell testing system. Humidified H_2 (~3%H_2O), as the fuel gas, was fed into the anode side at a flow rate of 60 mL min^{-1} [STP], while the cathode side was exposed to ambient air. The *I–V* polarization of the cell was measured from 700 to 500 °C, at 50 °C intervals, employing a Keithley 2420 digital source meter in a 4-probe mode.

2.4. Characterization techniques

The as-synthesized samples were characterized by room-temperature X-ray diffraction (XRD) for phase identification using a Philips X'pert diffractometer (Cu Ka radiation, $\lambda = 1.5418$ Å) in Bragg–Brentano reflection geometry, recorded in the 2θ range of 10–90° with an increment of 0.02°. The sintering behavior of the various samples was investigated by dilatometer curves, tested in air from room temperature to 1400 °C at a heating rate of 5 °C min^{-1} using a NETZSCH DIL 402C dilatometer. The morphology of the sintered electrolyte pellets and tested single cell were investigated by scanning electron microscopy (SEM, Model QUANTA-200).

Hydrogen temperature-programmed reduction (H_2-TPR) was carried out in a U-type quartz tube reactor to identify the chemical reduction properties of all the samples. Approximately 0.02 g of sample with a 40–60 mesh size was loaded in a U-type quartz tube and pretreated under a 10%H_2 in helium atmosphere at a flow rate of 30 mL min^{-1} for 30 min at room temperature. The temperature was then increased from room temperature to 930 °C at a ramp rate of 10 °C min^{-1}. The consumption of hydrogen was monitored by an in situ thermal conductivity detector (TCD) using a BELCAT-A apparatus.

X-ray photoelectron spectroscopy (XPS) was employed to investigate the chemical bonding state of Pd 3d, and the measurements were performed on a PHI 5000 Versaprobe system using monochromatic Al KR radiation (1486.6 eV). All the binding energies (BE) were referenced to the C 1s peak at 283.6 eV. The microstructure was also investigated by TEM. Powder samples for examination by transmission electron microscopy (TEM) were prepared by dispersing in ethyl alcohol, which acted as a dispersing agent, followed by ultrasonic treatment for 6 h; next, 4–6 drops of the suspension were placed on carbon films and dried for examination. Flake specimens for STEM analysis were prepared by ultrasonic cutting, mechanical thinning, polishing, dimpling, and Ar-ion milling using a Gatan Duo-mill (Gatan, Warrendale, PA, USA) at 0.5 mA and 4 kV. TEM and bright-field STEM images were obtained by an FEI Tecnai G2T20 electron microscope operating at 200 kV. EDX mappings were obtained by an FEI Tecnai G^2 F30 S-TWIN field emission transmission electron microscope equipped with EDAX energy-dispersive X-ray spectroscopy operating at 300 kV.

Thermogravimetric analyses (TGA, Model STA 449 F3, NETZSCH) of the hydrated samples were performed to quantify the protonic defects. Hydration of the powders was carried out in a tube furnace. The powders were first dried at 1000 °C for 2 h and then cooled down to room temperature under flowing Ar gas. Afterward, the dried powders were treated under wet Ar gas at a rate of 100 mL min^{-1} at 1000 °C for 2 h and then cooled down by steps of 2 °C min^{-1} until the temperature reached 200 °C. The cycle was repeated again from 800 to 200 °C to increase the hydration levels of the powders.

3. Results and discussion

3.1. Phase composition

It is well-known that some unusual valence states of cations can be stabilized in a perovskite structure, even some that are not possible as single oxides. For example, some precious metal elements such as Pd were found to be able to dope into the perovskite lattice structure and stabilize their ionic state at elevated temperature. In a previous study, Seshadri et al. demonstrated the synthesis of $BaCe_{1-x}Pd_xO_{3-\delta}$ using a solid-state reaction applying BaO_2, CeO_2 and PdO as raw materials in a pure oxygen atmosphere [42]. Via a sol–gel synthesis, the various cations were mixed homogeneously at an atom level: the long-distance solid-state diffusion of cations and anions for the formation of perovskite oxide was eliminated, thus benefiting the phase formation at lower temperature and enabling the synthesis of Pd-incorporated perovskite under an ambient air atmosphere.

Fig. 1a shows the room-temperature XRD patterns of $BaCe_{0.9}Y_{0.1}O_{3-\delta}$ (BCY), $BaCe_{0.8}Y_{0.1}O_{3-\delta}$ (BCY-non) and $BaCe_{0.8}Y_{0.1}Pd_{0.1}O_{3-\delta}$ (BCYP10) synthesized in air via the sol–gel process; both the BCY and the BCY-non samples were prepared by the calcination of their precursors from the sol–gel process at 1000 °C for 5 h. The crystal lattice parameters of BCY, BCY-non and BCYP10 were 73.76, 72.83 and 73.74 $Å^3$, respectively. For the stoichiometric BCY, all of the diffraction peaks can be easily indexed based on the perovskite structure with an orthorhombic symmetry, in good agreement with the literature results [43], suggesting the formation of a pure phase BCY oxide. For the B-site cation deficient BCY-non sample, the diffraction patterns were similar to that of the stoichiometric BCY without a noticeable shift of the diffraction peaks, suggesting that they have similar lattice parameters. For the BCYP10 sample, all of the diffraction peaks can also be indexed based on a perovskite structure, in addition to the main perovskite phase, impurities of CeO_2, PdO and Ba_2PdO_3 in low concentrations also appeared. In addition, no obvious shifts of the peak positions were observed compared to the stoichiometric BCY, which may be explained by the similar ionic radius of the six-coordinated Pd^{2+} ion (0.86 Å) and Ce^{4+} ions (0.87 Å). To determine the capability of Pd egress from the perovskite host, BCYP10 was treated under a flowing 10%H_2–Ar atmosphere at 1000 °C for 2 h. The XRD patterns for BCYP10 before and after the treatment in the reducing atmosphere are compared in Fig. 1b. For the treated BCYP10, a new diffraction peak at 2θ around 40.1° appeared, which can be assigned to the (111) reflection of fcc Pd0. This result suggests that the Pd in BCYP10 was successfully reduced and segregated after treatment at 1000 °C in a dilute hydrogen atmosphere.

To further demonstrate the successful egress of Pd, the sample BCYP10 after the treatment in hydrogen at 1000 °C was submitted

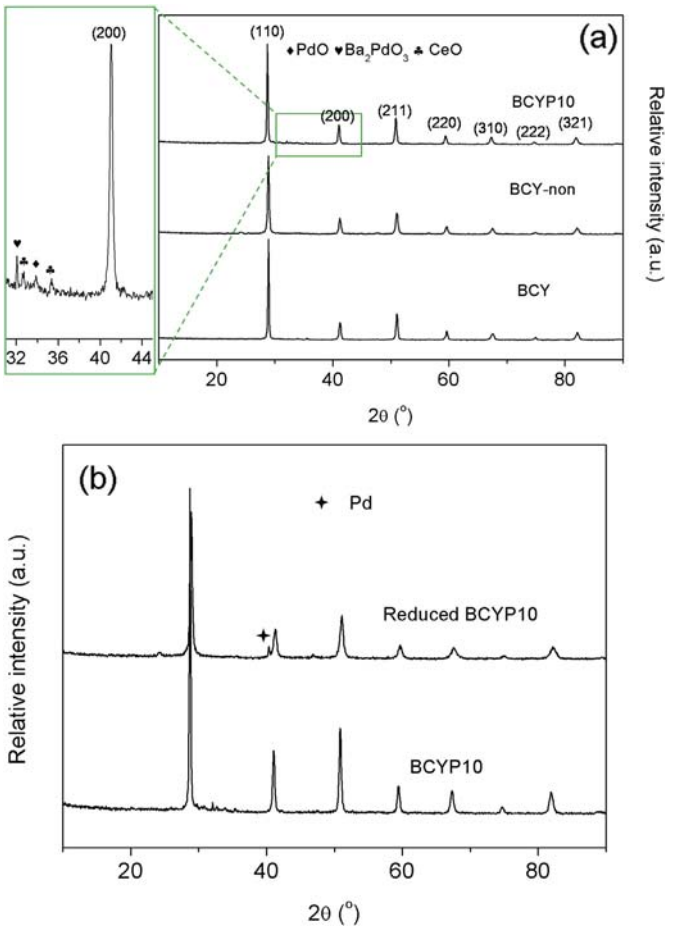

Fig. 1. XRD patterns of (a) BCY, BCYP10 and BCYP-non and (b) reduced BCYP10 under 10%H_2–Ar atmosphere at 1000 °C.

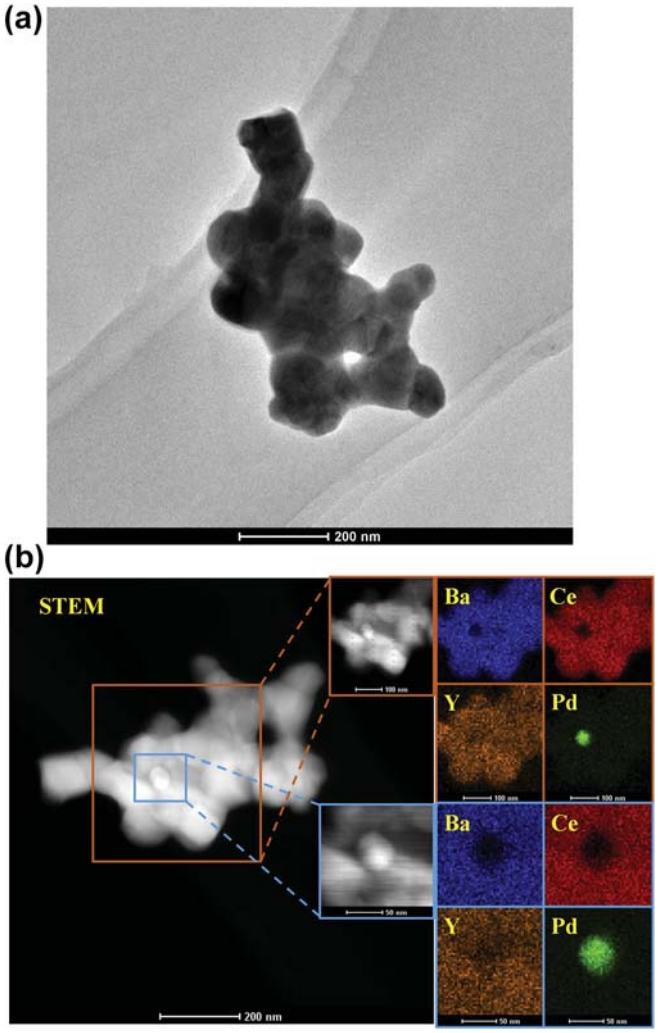

Fig. 2. TEM images of a BCYP10 nanoparticle after sintered at 1000 °C in flowing 10% H_2–Ar atmosphere. (b) STEM image and the corresponding EDX elemental distribution of Ba, Ce, Y and Pd in reduced BCYP10.

for TEM and STEM observation. Fig. 2a shows a typical TEM image. The primary particles were spherical in shape with a size of 50–100 nm, which were agglomerated to form secondary particles with a size of 200–500 nm. Fig. 2b shows the corresponding STEM image and energy dispersive X-ray (EDX) elemental mapping. For most of the aggregates, a homogeneous distribution of Ba, Ce and Y was observed. Around the grain boundaries of several particles, the element mapping demonstrated the existence of a particular particle composed of only Pd, spherical in shape with a size of approximately 40 nm. This observation strongly supports the successful egress of Pd from the oxide lattice, where it decorates the grain boundary of the perovskite host particles. A similar phenomenon was also discovered by others [39–44], but the particles in these studies are only 1–3 nm. The much larger Pd particle size observed in this study can be ascribed to the high calcination temperature.

To obtain further structural information, the oxidation state of Pd was analyzed by core-level X-ray photoelectron spectroscopy (XPS). The XPS spectra of the as-prepared and reduced BCYP10 samples in the region of the palladium 3d binding energies are presented in Fig. 3a, corrected based on the measured values for C 1s. The XPS curves were fitted with Pd $3d_{5/2}$ (337.3 eV) and Pd $3d_{3/2}$ (342.6 eV), indicating that Pd^{2+} ions were mainly present in BCYP10. However, these peak positions shifted to a higher binding energy, by approximately 0.6 eV, with respect to normal PdO and were close to the binding energies of $PdCl_2$ and $Pd(NO_3)_2$. [45,46] A similar shift toward higher binding energy was also found in $BaCe_{1-x}Pd_xO_{3-\delta}$ materials, highly dispersed Pd/Al_2O_3, and $Ce_{1-x}Pd_xO_{2-\delta}$ solid solution, [39,47,48] suggesting that the Pd^{2+} ions in BCYP10 were much more ionized than those in PdO. Nishihata et al. interpreted the shift in binding energies of palladium in perovskites to the existence of Pd^{3+}; [38] nevertheless, the most likely Pd oxidation state in $BaCe_{1-x}Pd_xO_{3-\delta}$ was still Pd^{2+}, supported by computational investigation. [49] Li and co-workers further discovered a doublet of palladium 3d peaks based on Pd^0 in $BaCe_{0.9}Pd_{0.1}O_{3-\delta}$. [42] In this study, no Pd^0 was observed in the BCYP10 sample, likely due either to the sol–gel process facilitating the formation of the perovskite structure at reduced temperature and stabilizing the Pd^{2+} in the perovskite lattice or to the limited sensitivity of XPS. Further investigation is required, which is discussed later. After the treatment in flowing 10%H_2–Ar atmosphere at 1000 °C for 2 h, as shown in Fig. 3a, the spectra of Pd_{3d} in BCYP10 can be resolved into two sets of spin–orbit doublets, which were attributed to Pd^0 (335.0 eV and 340.1 eV) and Pd^{2+} (337.7 eV and 343.6 eV). However, the peak intensity of Pd^{2+} was very low, suggesting a low concentration of Pd^{2+}. Thus, most of the Pd^{2+} in the sample was likely reduced to Pd^0, which agrees with the observation of Pd nanoparticles by STEM. As fuel cell electrolytes, the material should be sintered at an elevated temperature, usually 1400–1600 °C, to achieve sufficient densification. Fig. 3b shows the

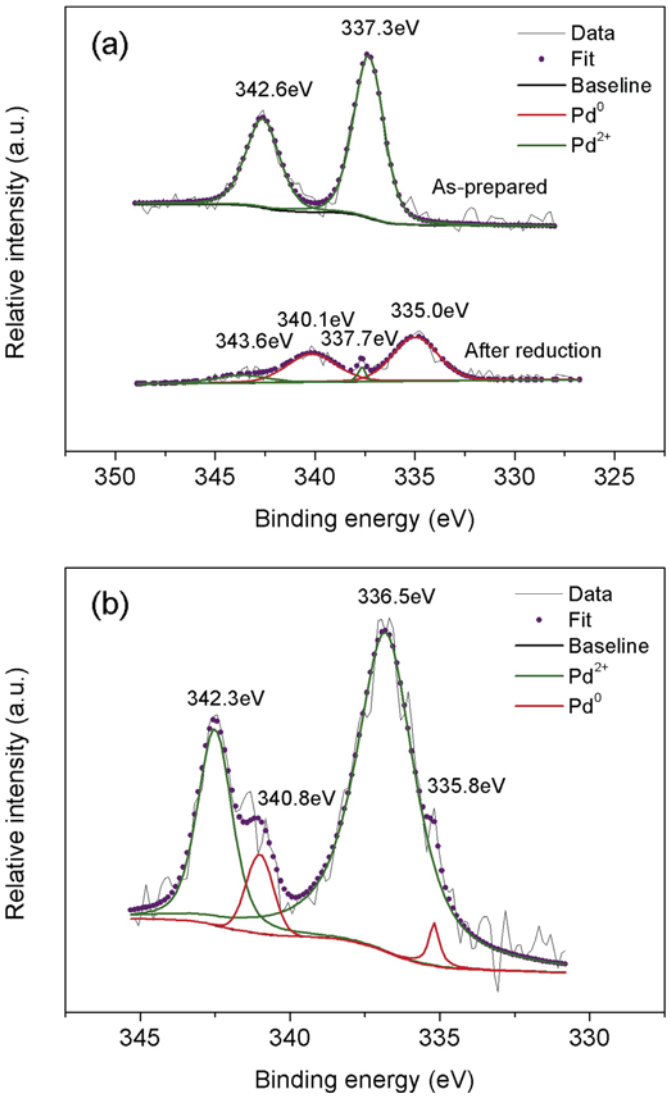

Fig. 3. (a) XPS spectra in the palladium 3d region of as-prepared BCYP10 and the spectrum corresponds to the sample of reduced BCYP10. (b) XPS spectra in the palladium 3d region of BCYP10 after sintering at 1400 °C.

XPS spectra in the palladium 3d region of BCYP10 after the sintering at 1400 °C in air. In addition to the peaks at 342.3 and 336.5 eV, which were assigned, respectively, to Pd $3d_{5/2}$ and Pd $3d_{3/2}$ of Pd^{2+}, two shoulder peaks at 340.8 and 335.8 eV also appeared, which can be assigned to Pd $3d_{5/2}$ and Pd $3d_{3/2}$ of Pd0. This result suggests that the Pd^{2+} in the perovskite lattice was thermally reduced and released as metallic Pd under the high temperature sintering conditions. Such a process may benefit the membrane sintering, which is discussed later.

XRD is insensitive to well-dispersed species inside a sample, while as a surface probing technique, XPS can provide information on the valence state of surface ions and TEM can only give morphological and structural information of the local environment. Thus, it is still difficult to determine precise concentrations of Pd^{2+} and Pd^0 inside the bulk oxides. It is well known that metallic Pd can adsorb hydrogen at room temperature and release it at higher temperature, while Pd^{2+} can be reduced by hydrogen at elevated temperature. Based on the above features, it is possible to determine the relative amount of Pd^{2+} and Pd^0 inside the BCYP sample using the H_2 temperature-programmed reduction (H_2-TPR) technique. By first treating the sample in a hydrogen atmosphere at room temperature and then linearly increasing the temperature under the same atmosphere, any hydrogen adsorbed by the Pd^0 at room temperature will be released at a higher temperature to give a negative peak, while the reduction of Pd^{2+} to Pd will consume the hydrogen to result in positive hydrogen consumption peaks in the H_2-TPR profile. Based on the area of the hydrogen adsorption and consumption peaks, precise information about the concentration of Pd^{2+} and Pd^0 in the sample may be obtained. Fig. 4 shows the H_2-TPR profiles of the as-prepared BCY, BCYP10, BCYP10-1400 and BCYP10-reduced. For the BCY sample, no reduction peak was observed at temperatures lower than 300 °C, while three successive reduction peaks appeared at approximately 440, 630 and 800 °C, which were related to the reduction of Ce^{4+} to Ce^{3+} in the lattice. For BCYP10, a sharp hydrogen desorption peak was observed at 95 °C, which is the characteristic peak for hydrogen release from pre-adsorbed Pd, suggesting the presence of metallic Pd in BCYP10, which was not detectable by XPS and XRD. From 200 to about 380 °C, strong and broad hydrogen consumption peaks were present (though such peaks were not observed in BCY), and they were then assigned to the reduction of Pd^{2+} to Pd^0. The correlation of the strong hydrogen desorption peak at 95 °C to the Pd metal, and the broad hydrogen consumption peaks from 200 to 380 °C to the reduction of Pd^{2+} was further supported by the disappearance for the peaks in the 200–380 °C range, while the peak at 95 °C was significantly strengthened in intensity for BCYP10 after the pre-reduction in hydrogen at room temperature for 0.5 h before conducting the H_2-TPR experiment. The amount of Pd^0 in the sample can be quantitatively determined by the area of the hydrogen desorption peak at 95 °C, assuming that all of the Pd^{2+} was successfully reduced in the sample pre-reduced in a hydrogen atmosphere. Approximately 5.6% of the Pd in BCYP10 was in the Pd^0 oxidation state, while the remaining 94.4% Pd was doped into the perovskite lattice as Pd^{2+}. With the increase of the calcination temperature, an increasing concentration of Pd^0 was observed. For the BCYP10-1400 sample, the Pd^0 percentage increased to 36.7% based on the H_2-TPR results, suggesting that the Pd^{2+} in the perovskite was largely reduced after the sintering at 1400 °C. This result implies that the Pd^{2+} in the perovskite lattice was not thermodynamically stable at 1400 °C, although the Pd^{2+} did survive in the perovskite lattice at 1000 °C in air.

To determine the effect of the incorporation of Pd on the sintering behavior of BCYP10, cation stoichiometric BCY and BCYP10

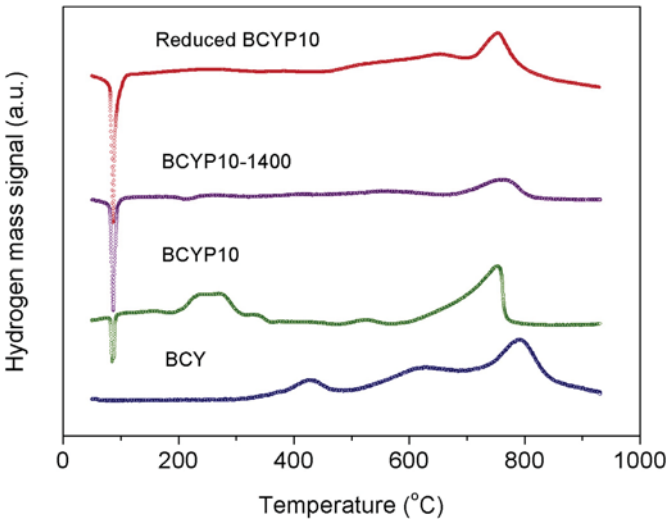

Fig. 4. H_2-TPR profiles of as-prepared BCY, BCYP10-1, BCYP10-2, BCYP10-1400 and reduced BCYP10.

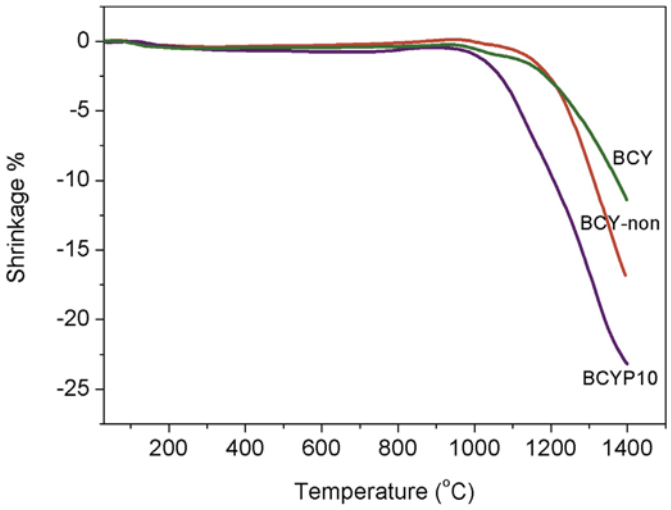

Fig. 5. Dilatometric curves of BCY, BCYP10 and BCY-non green pellets.

were comparatively studied using dilatometric measurements. During the experiment, the green pellets were heated at a rate of 5 °C min^{-1} in air, and the dimensional change was recorded in situ. The complete egress of Pd from the perovskite lattice would lead to the formation of a B-site cation deficient BCY, i.e., BCY-non, which was also synthesized and investigated by dilatometry for comparison. As shown in Fig. 5, the incorporation of Pd significantly enhanced the sintering of BCY. The onset temperature for the sintering of BCYP10 occurred at approximately 950 °C, which was approximately 100 °C lower than that of cation stoichiometric BCY. From 900 to 1200 °C, the shrinkage of BCYP10 reached 9.8%, compared to 3.1% for the cation stoichiometric BCY. The final shrinkage (1400 °C) of BCYP10 reached 23.2%, whereas it was only 12.1% for BCY and approximately 16.9% for BCY-non. This finding suggests that the B-site cation deficiency also aided the sintering of the BCY ceramic because it likely contributes to the formation of additional oxygen vacancies, which facilitate oxygen diffusion during sintering. Based on the data of sintering curves, the sintering densification temperature of BCYP10 was calculated was 1329 °C, while that of BCY-non and BCY exceeded 1400 °C. At any rate, the presence of Pd clearly facilitated the sintering of the ceramic. The initial relative densities of BCYP10, BCY-non and BCY were 52.7%, 52.3% and 52.6%, respectively. Therefore, the effects of initial densities on the sintering shrinkage can be neglected.

The improved sintering with the incorporation of Pd was further supported by direct microscopic observation. Fig. 6 shows the SEM images of BCYP10, BCY and BCY-non after sintering at 1400 °C in air for 5 h. For the BCYP10 membrane, well-sintered bulk was observed with almost no pinholes or enclosed holes. Grains 5–10 μm in size were fused together. For the BCY membrane, the grains showed a much smaller size of 2–5 μm, and a considerable amount of enclosed pores with a diameter of 3 μm were observed. Thus, in the literature, a calcination of 1500 °C was usually applied to achieve affordable densification for self-supported thick BCY ceramics [50]. For the BCY-non membrane, it was much better sintered compared to the cation stoichiometric BCY, and this result is in good agreement with the dilatometric results; this finding is explained by the creation of additional oxygen vacancies from the B-site cation deficiency. Noticeable amounts of irregular enclosed pores were still observed in the bulk. A comparison of SEM images of the three membranes further supported that Pd facilitated the sintering of perovskite oxide. Fig. 7 shows the STEM images and EDX elemental mapping of a local region of BCYP10 pellets after sintering at 1400 °C. Two Pd nanoparticles located in the grain boundary regions were observed, providing further support for the egress of Pd from the oxide lattice during the high-temperature sintering process.

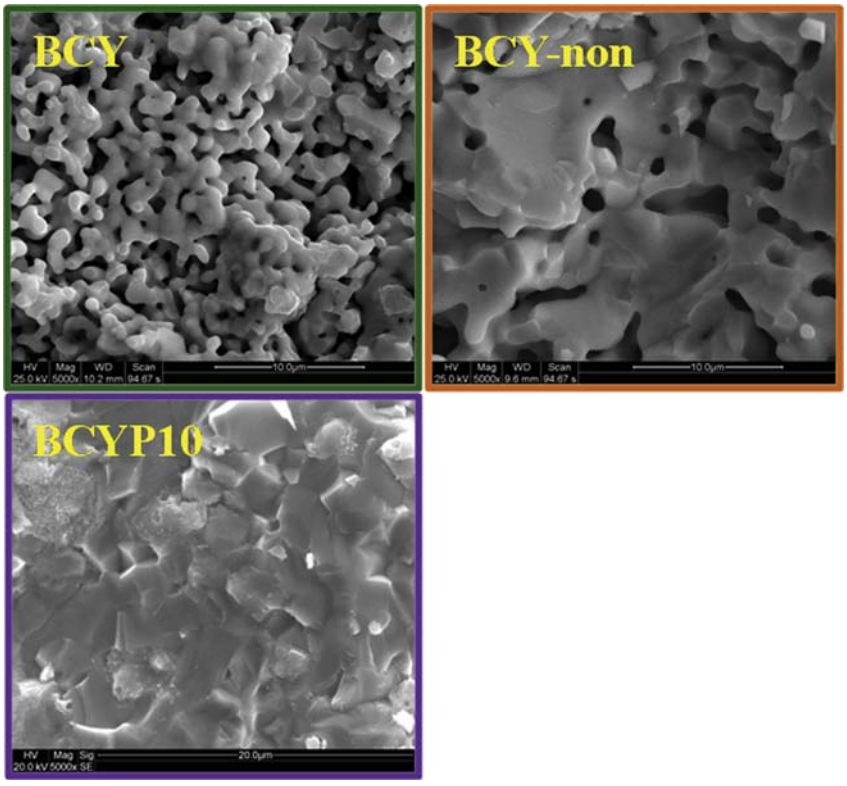

Fig. 6. The fracture surface SEM imaging of BCY, BCYP10 and BCY-non after sintering at 1400 °C.

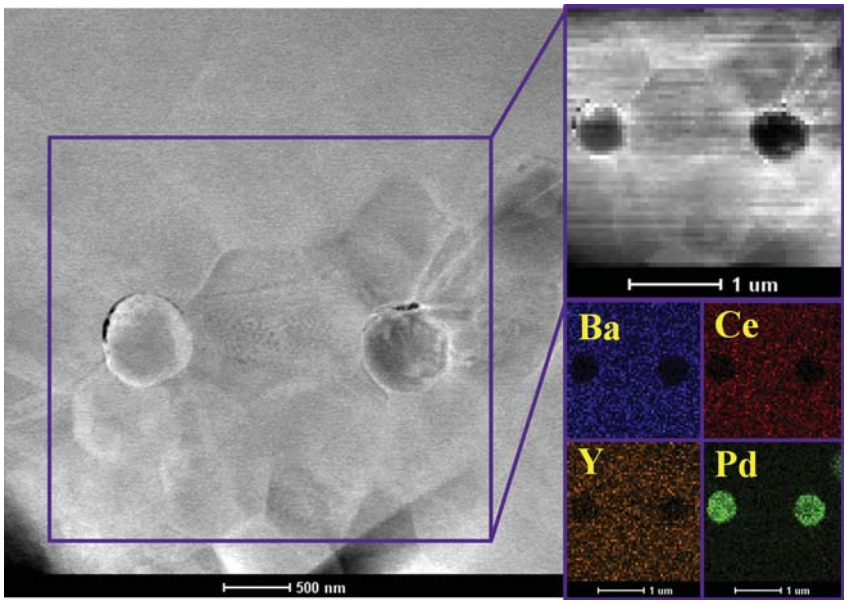

Fig. 7. STEM image and the corresponding EDX elemental distribution of Ba, Ce, Y and Pd in BCYP10 pellets after sintering at 1400 °C.

Based on the above results, a mechanism for the improved sintering of BCY electrolyte after the incorporation of Pd was proposed and is shown in Fig. 8a. The presence of Pd in the oxide lattice reduced the bonding energy of oxygen with the cations and increased the oxygen mobility inside the oxide lattice, thus improving the sintering of the BCY membrane at the early stage. This situation was demonstrated by the XPS spectrums of O 1s in Fig. 8b. After reducing BCYP10, the binding

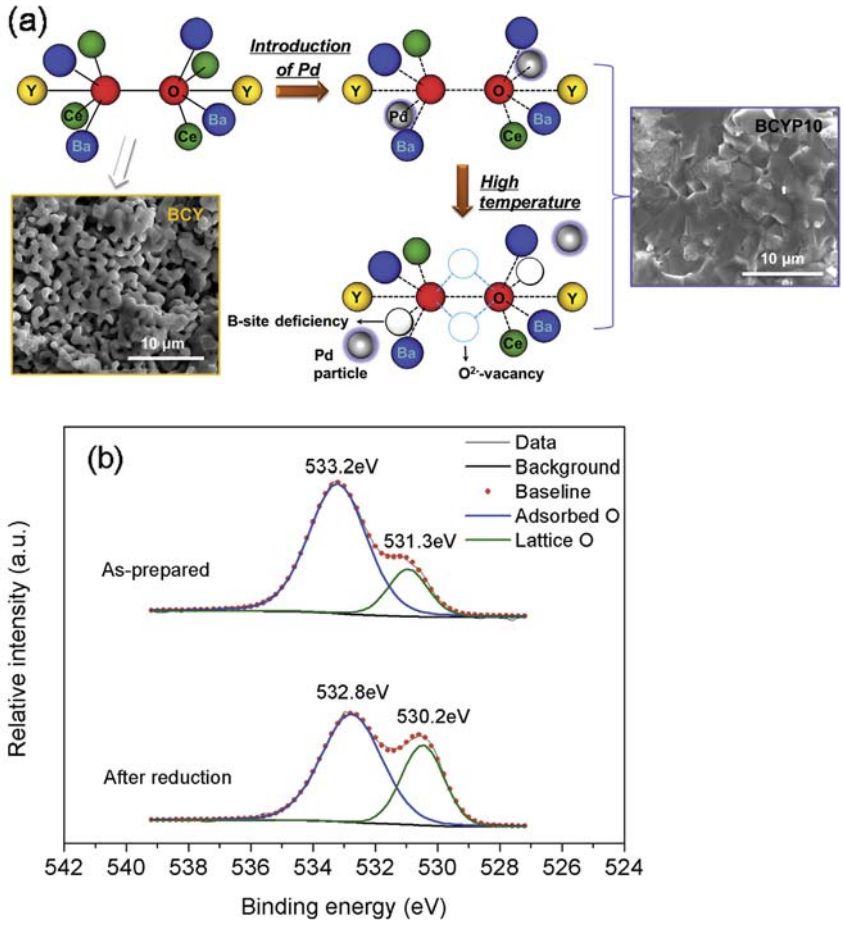

Fig. 8. Schematic mechanism for the improved sintering of BCY electrolyte after the incorporation of Pd.

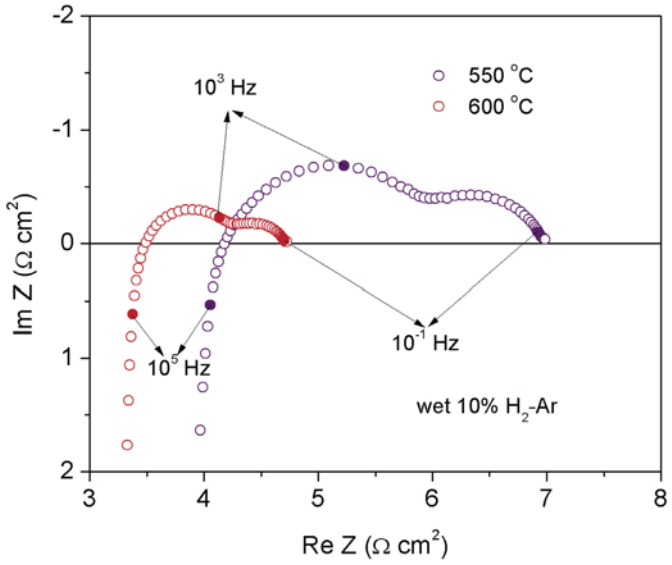

Fig. 9. The impedance spectra of BCYP10 at 550 °C and 600 °C in wet 10%H_2–Ar atmosphere.

energy of oxygen in lattice was dropped from 531.3 eV to 530.2 eV. With increasing temperature, Pd was progressively released from the oxide lattice to create a B-site cation deficient BCY and Pd nanoparticles. The B-site cation deficiency promoted the formation of oxygen vacancies and facilitated the sintering on the one hand, and the Pd likely performed as a sintering aid on the other hand; as a result, a noticeable improvement in the sintering was observed.

3.2. Proton conductivity

The conductivity of BCY and BCYP10 pellets in wet air and wet 10%H_2–Ar atmospheres from 750 to 200 °C were measured using EIS. Because the depletion of Pd from the lattice leads to the formation of a B-site cation deficient perovskite, the conductivity of the cation-deficient $BaCe_{0.8}Y_{0.1}O_{3-\delta}$ (BCY-non) was also measured for comparison. Fig. 9 shows the representative EIS complex plane plots for BCYP10 at 550 and 600 °C in a wet 10%H_2–Ar atmosphere. The EIS are composed of two suppressed semiarcs, located at the intermediate frequency and low frequency ranges, which are related to the grain boundary conduction and electrode reaction, respectively. Fig. 10 shows the total conductivity as a function of temperature in the Arrhenius plots for the various dense samples under wet air and wet 10%H_2–Ar atmosphere from 750 °C to 200 °C. To obtain the dense structures, BCYP10, BCY-non and BCY green pellets were sintered at 1400 °C, 1500 °C and 1500 °C for 5 h, respectively.

Under a wet air atmosphere, the following reaction occurs:

$$H_2O + V_O^{\cdot\cdot} + O_O^x \rightarrow 2(OH)_O^{\cdot}$$

Both $V_O^{\cdot\cdot}$ and O_O^x are present in the oxides; the materials could thus be a mixed oxygen ion and proton conductor. According to Fig. 10, the total conductivity was the highest for BCYP10, followed by cation deficient BCY-non, while the cation stoichiometric BCY had the lowest conductivity. Typically, the activation energy for proton diffusion and oxygen transport is from 0.3 to 0.6 eV and 1.0 to 1.2 eV, respectively. The large ionic size of the oxygen ion results in the high activation energy associated with oxygen transport. The activation energy for the conductivity in wet air was calculated to be 0.56, 0.57 and 0.58 eV for BCYP10,

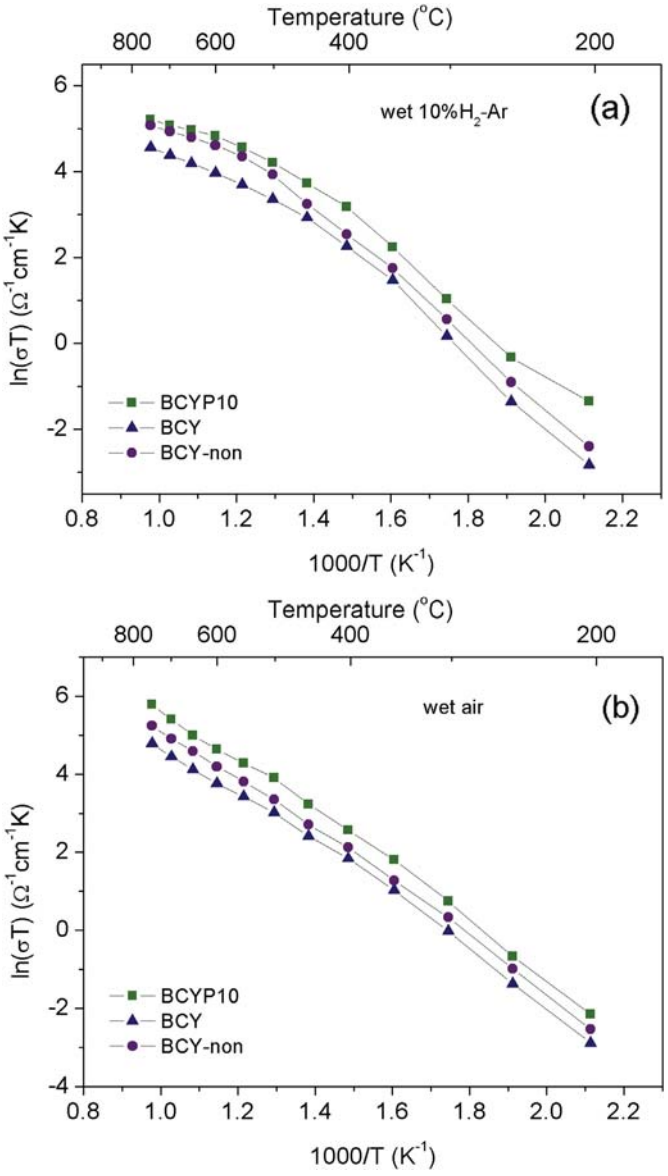

Fig. 10. Temperature dependence of total conductivity of BCY, BCYP10 and BCY-non in Arrhenius plots under (a) wet 10%H_2–Ar, (b) wet air atmosphere.

BCY and BCY-non, respectively. This result suggests that the species being conducted in the above materials under wet air and intermediate temperature conditions is mainly the proton. The higher conductivity of BCY-non than BCY suggests that the introduction of cation vacancies improved the proton conductivity.

According to Eq. (1), the formation of protonic defects was accompanied by a significant increase in weight; thus, the concentration of protonic defects can be quantitatively analyzed by TGA. Fig. 11 shows the TGA curves of the hydrated BCY and BCYP10 samples prepared at 1000 °C. Assuming full hydration of the structures and that all Pd is present as Pd^{2+} in the B-site of the perovskite lattice, a maximum $^{\cdot}OH$ defect concentration of 0.1 and 0.3 should be formed for cation stoichiometric BCY and BCYP10, respectively. Based on the TGA data, the corresponding values are 0.109 and 0.328. The higher measured values suggest that some Pd^{2+} was likely released from the oxide lattice to create cation vacancies, which facilitated the formation of additional oxygen vacancies for charge neutrality, in agreement with the H_2-TPR

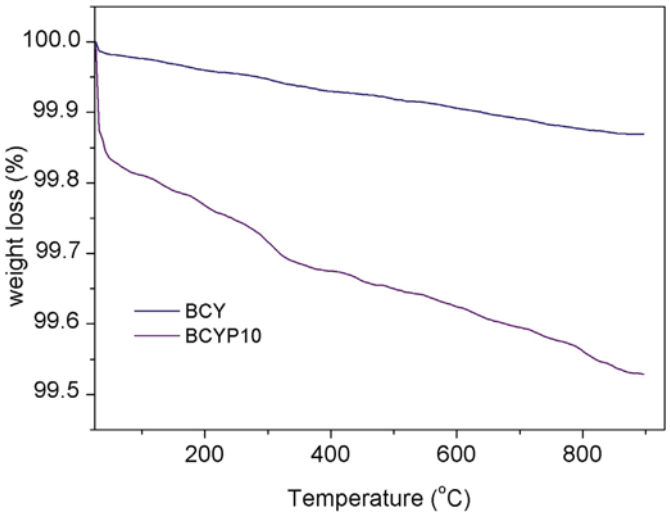

Fig. 11. Thermogravimetric analysis of the hydrated BCY and BCYP10.

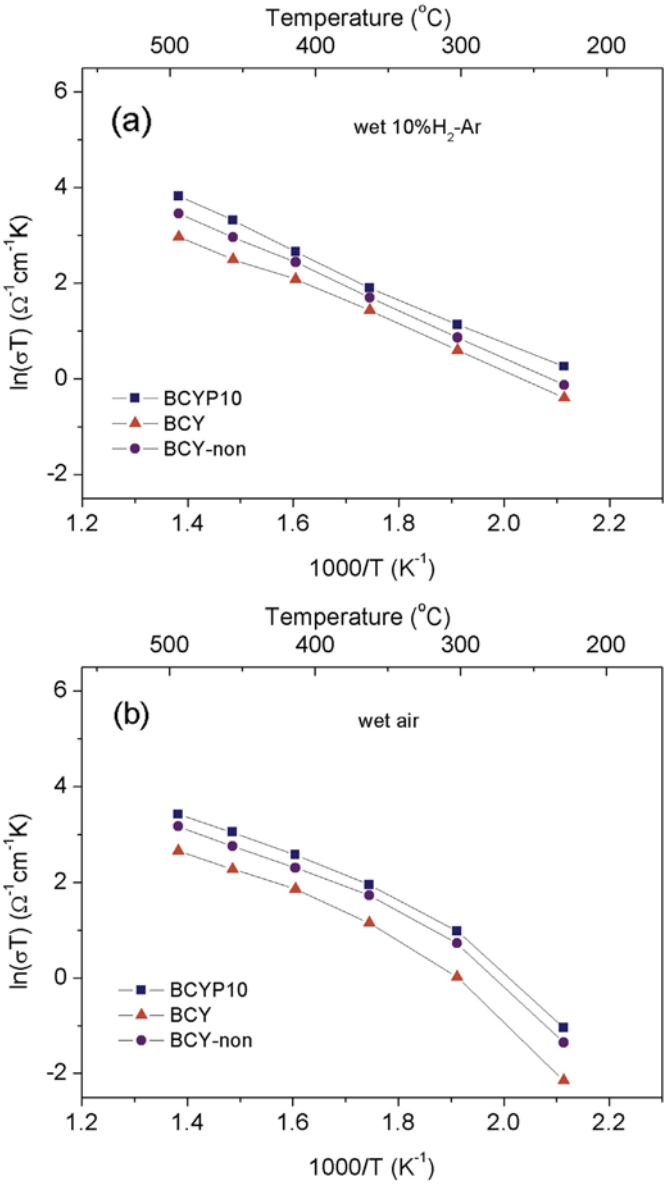

Fig. 12. Temperature dependence of bulk conductivity of BCY, BCYP10 and BCY-non in Arrhenius plots under (a) wet 10%H_2–Ar, (b) wet air atmosphere.

results. The high $^{\bullet}OH$ defect concentration contributed in part to the excellent electrical conductivity of BCYP10.

As demonstrated from the TGA, the formation of cation vacancies increased the $^{\bullet}OH$ defect concentration and thus facilitated the proton diffusion inside the oxide lattice. Under a humidified 10%H_2–Ar atmosphere, the defect reaction can be written as Eq. (1). This finding suggests that proton and oxygen ion conduction could occur simultaneously under a reducing atmosphere. The activation energies in a wet 10%H_2–Ar atmosphere were found to be 0.52, 0.54 and 0.56 eV for BCYP10, BCY and BCY-non, respectively, suggesting that the proton was still the main species being conducted under a reducing atmosphere.

As mentioned, the electrical conductivity in BCY and BCYP10 was a result of both the bulk and grain boundary conductivity, which can be separated in EIS from the high frequency arc and intermediate frequency arc. Fig. 12 shows the bulk conductivity in wet air and wet 10%H_2–Ar atmospheres for BCY, BCY-non, and BCYP10. The incorporation of Pd improved the bulk conductivity under both wet air and wet 10%H_2–Ar atmospheres. In this case, the introduction of Pd led to the formation of additional oxygen vacancies, which played a crucial role in the formation of mobile protons. Fig. 13 shows the grain boundary conductivities of BCYP10. The excellent grain boundary conductivity of BCYP10 in wet 10%H_2–Ar gas was responsible for its high total conductivity under the same conditions. With fitting of impedance spectra, the capacitance for grain boundary of BCY-non and BCYP10 were 8.76×10^{-9} F and 6.23×10^{-9} F at 450 °C, which may be attributed to the Pd particles in some grain boundary regimes. Moreover, the capacitance for grain boundary of BCY-non and BCYP10 are always around 10^{-9}.

To investigate the effects of a B-site defect structure, which was created from the extraction of Pd particles under high temperature, on the conductivity of BCYP10, the conductivity of BCY-non was also measured under the same conditions that were used to measure the BCYP10 pellets. The total, bulk, and grain boundary conductivities of BCY-non under wet air and wet 10% H_2–Ar atmospheres are displayed as a function of temperature in Arrhenius plots from 200 to 750 °C in Figs. 10, 12 and 13, respectively. The bulk conductivity of BCY-non in the different atmospheres was close to that of BCYP10 and was higher than BCY. This result highlights the positive influence of the cation non-stoichiometry on the bulk conductivity because the formation of additional oxygen ion vacancies enhanced the ion mobility and the quantity of mobile ions. However, the grain boundary conductivity of Pd-free BCY-non pellets was poorer than that of BCYP10. Such a phenomenon demonstrated that the Pd egress had a beneficial effect on the grain boundary conductivity. Overall, the influence of the non-stoichiometric structure on the bulk conductivity and the effect of the Pd nanoparticles on the grain boundary conductivity synergistically enhanced the total conductivity of BCYP10. The capacity for hydrogen adsorption of Pd and its catalytic activity in hydrogen dissociation may also play a positive role in the improved protonic conductivity of BCYP10 [51].

3.3. Fuel cell performance

The as-synthesized BCYP10 was applied as an electrolyte material and fabricated into a single cell in an anode-supported thin film electrolyte configuration for electrochemical performance testing. Fig. 14 shows the SEM image from a

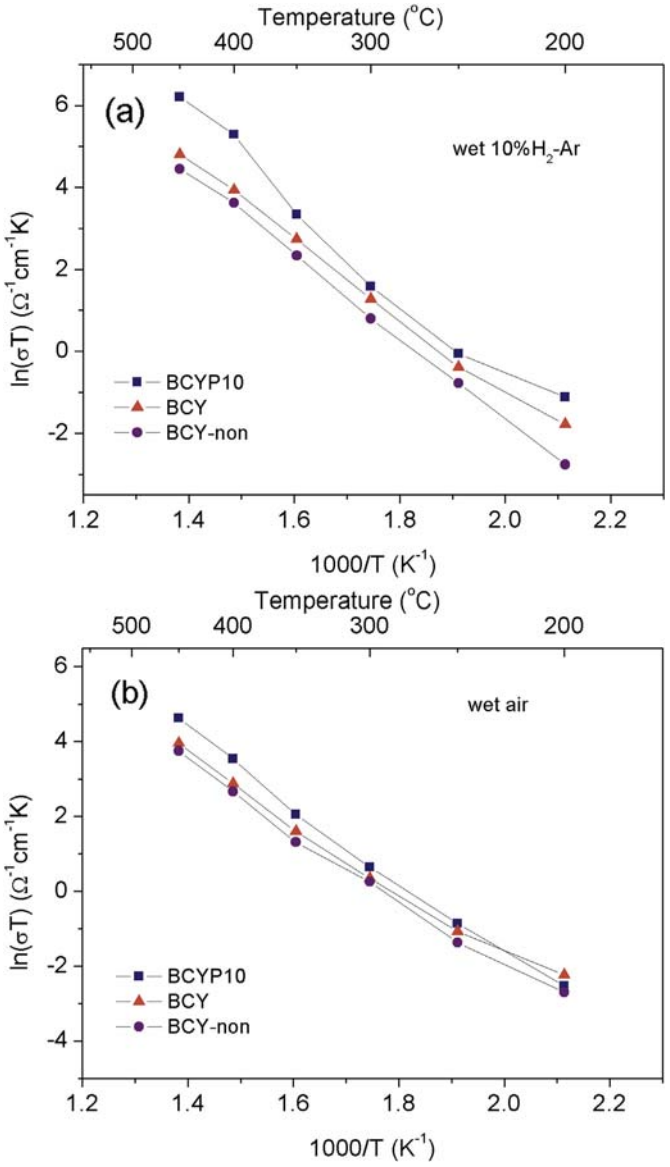

Fig. 13. Temperature dependence of grain boundaries conductivity of BCY, BCYP10 and BCY-non in Arrhenius plots under (a) wet 10%H_2–Ar, (b) wet air atmosphere.

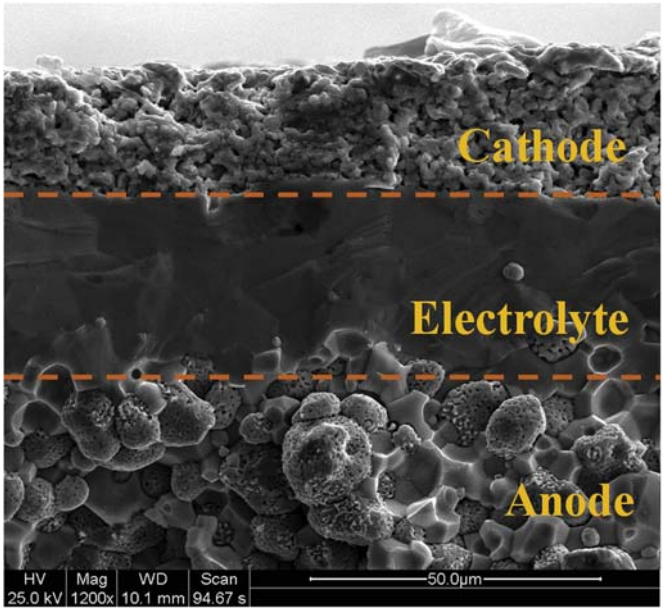

Fig. 14. SEM image from the cross-sectional view of the tested BCYP10-based single cell.

cross-sectional view of a typical single cell with a reduced BCYP10 + NiO anode and BSCF cathode, for which the anode-electrolyte dual layer cells were sintered at 1400 °C for 5 h. Although a relatively low sintering temperature (1400 °C) was selected in this study, the electrolyte layer, which has a thickness of approximately 30 μm, was well densified, without any pinholes and almost no enclosed pores, suggesting perfect sintering. The cell was then operated on ~3%H_2O humidified H_2 fuel while the cathode was exposed to ambient air. Fig. 15a shows the corresponding steady-state *I–V* and *I–P* polarization curves. Open circuit voltages (OCVs) of 1.101, 1.093, 1.079, 1.041 and 1.021 V were achieved at 500, 550, 600, 650 and 700 °C, respectively. For a similar cell with a thin film of cation stoichiometric $BaCe_{0.9}Y_{0.1}O_3$ (BCY) electrolyte and a BSCF cathode, the corresponding OCVs are 1.098, 1.072, 1.061, 1.047 and 1.023 V, respectively. The high OCVs of the cell with the BCYP10 electrolyte suggest that the formation of the Pd–BCY nano ionic composite did not significantly increase electronic the charge transfer number. This result can be explained by the fact that the Pd nanoparticles were isolated inside the electrolyte bulk, separate from the formation of the continuous path for electron conduction. Actually, slightly increased OCVs were even observed at corresponding temperatures for the cell with the BCYP10 electrolyte compared to that with the BCY electrolyte, likely due to the improved densification of the thin film electrolyte. Peak power densities (PPDs) of 199, 277, 357, 459 and 645 mW cm^{-2} were obtained at 500, 550, 600, 650 and 700 °C, respectively. The cell performance was much better than that reported by Guo et al., who used a similar BCY electrolyte and BSCF cathode [50]. For application point of view, the power density of fuel cell based on BCYP10 electrolyte at 0.7 V were 560, 401, 316, 247 and 177 mW cm^{-2} at 700, 650, 600, 550 and 500 °C, respectively. EIS of the SOFC under the OCV condition were also measured, with the results shown in Fig. 15b. The intercept of the impedance spectra at high frequency with the real axis represents the ohmic resistance, whereas the intercept at low frequency with the real axis corresponds to the total resistance of the cell. The difference between the intercepts at high and low frequencies is the electrode polarization resistance, which is a sum of the resistance of the two interfaces, i.e., the cathode/electrolyte interface and the anode/electrolyte interface. The ohmic resistances were only 0.46, 0.73 and 1.14 Ω cm^2 at 700, 600 and 500 °C, respectively. This finding further demonstrates the good conductivity of the BCYP10 electrolyte. However, the electrode polarization resistance was increased more significantly than the ohmic resistance of the cell with the decrease in the operation temperature. Thus, a further significant increase in the performance of the SOFC based on the BCYP10 electrolyte is expected if a favorable cathode is developed.

4. Conclusions

Pd-doped BCY perovskite oxides were successfully synthesized using an EDTA–citrate complexing sol–gel method. Doping the B-site with Pd had a positive effect on the sintering behavior. The egress of the Pd ion from the oxide lattice modified the surface of the perovskite structure with Pd nanoparticles under reducing

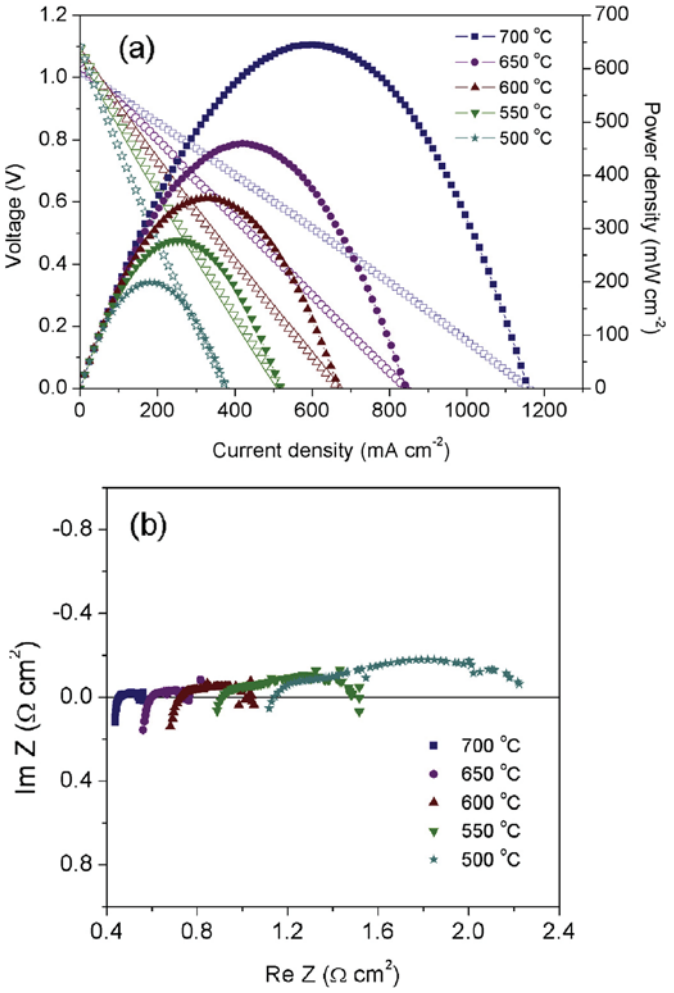

Fig. 15. (a) *I–V* and *I–P* curves for a single cell with a configuration of BCYP10–Ni/BCYP10/BSCF; (b) Electrochemical impedance spectra of the single cell with BCYP10-based electrolyte under open-circuit condition.

conditions or high temperature. After the decoration of the perovskite surface with Pd, the capacity for proton incorporation at high temperature was significantly enhanced, giving birth to the excellent protonic conductivity of BCYP10. Both the B-site defect structure and the Pd nanoparticles were responsible for the enhanced total conductivity of BCY. The improved sintering and enhanced ionic conductivity resulted in a high power output of the cell with the BCYP10 electrolyte, reaching a peak power density of 645 mW cm^{-2} and an OCV of 1.021 V at 700 °C. The development of a more favorable cathode material could further improve the performance of fuel cells with BCYP10, making them highly attractive with considerable potential in practical application.

Acknowledgments

This work was supported by the " National Science Foundation for Distinguished Young Scholars of China" under contract No. 51025209.

References

[1] T. Hibino, A. Hashimoto, M. Yano, M. Suzuki, S. Yoshida, M. Sano, J. Electrochem. Soc. 149 (2002) A133–A136.
[2] H. Yokokawa, N. Sakai, T. Horita, K. Yamaji, Fuel Cells 1 (2001) 117–131.
[3] Y. Shao, F. Ding, J. Xiao, J. Zhang, W. Xu, S. Park, J. Zhang, Y. Wang, J. Liu, Adv. Funct. Mater. 23 (2013) 987–1004.
[4] M.D. Slater, D. Kim, E. Lee, C.S. Johnson, Adv. Funct. Mater. 23 (2013) 947–958.
[5] J.M. Tarascon, M. Armand, Nature 414 (2001) 359–367.
[6] W.C. Chueh, F.E. Gabaly, J.D. Suger, N.C. Bartelt, A.H. McDaniel, K.R. Fenton, K.R. Zavadil, T. Tyliszczak, W. Lai, K.F. McCarty, Nano Lett. 13 (2013) 866–872.
[7] D.M. Bierschenk, J.R. Wilson, S.A. Barnett, Energy Environ. Sci. 4 (2011) 944–951.
[8] A. Lashtabeg, S.J. Skinner, J. Mater. Chem. 16 (2006) 3161–3170.
[9] W. Jung, J.O. Dereux, W.C. Chueh, Y. Hao, S.M. Haile, Energy Environ. Sci. 5 (2012) 8682–8689.
[10] A. Taramcón, S.J. Skinner, R.J. Chater, F. Hernández-Ramírez, J.A. Kilner, J. Mater. Chem. 17 (2007) 3175–3181.
[11] Q.F. Li, R.H. He, J.O. Jensen, N.J. Bjerrum, Chem. Mater. 15 (2003) 4896–4915.
[12] Z.P. Shao, S.M. Haile, J. Ahn, P.D. Ronney, Z.L. Zhan, S.A. Barnett, Nature 435 (2005) 795–798.
[13] W. Wang, C. Su, Y.Z. Wu, R. Ran, Z.P. Shao, Chem. Rev. 113 (2013) 8104–8151.
[14] T. Hibino, A. Hashimoto, T. Inoue, J. Tokuno, S. Yoshida, M. Sano, Science 288 (2000) 2031–2033.
[15] C. Su, W. Wei, R. Ran, Z.P. Shao, M.O. Tade, S.M. Liu, J. Mater. Chem. A 1 (2013) 5620–5627.
[16] Y. Liu, Y.M. Guo, W. Wei, C. Su, R. Ran, H.T. Wang, Z.P. Shao, J. Power Sources 196 (2011) 9246–9253.
[17] Q. Liu, X.H. Dong, G.L. Xiao, F. Zhao, F.L. Chen, Adv. Mater. 22 (2010) 5478–5482.
[18] C.H. Yang, Z.B. Yang, C. Jin, G.L. Xiao, F.L. Chen, M.F. Han, Adv. Mater. 24 (2012) 1439–1443.
[19] Y. Ma, X.D. Wang, S.H. Li, M.S. Toprak, B. Zhu, M. Muhammed, Adv. Mater. 22 (2010) 1640–1644.
[20] J.H. Shim, C.C. Chao, H. Huang, F.B. Prinz, Chem. Mater. 19 (2007) 3850–3854.
[21] H. Iwahara, H. Uchida, K. Ono, K. Ogaki, J. Electrochem. Soc. 135 (1988) 529–533.
[22] Y. Liu, Y.M. Guo, R. Ran, Z.P. Shao, J. Membr. Sci. 437 (2013) 189–195.
[23] L. Yang, C.D. Zuo, S.Z. Wang, Z. Cheng, M.L. Liu, Adv. Mater. 20 (2008) 3280–3283.
[24] C.D. Zuo, S.W. Zha, M.L. Liu, M. Hatano, M. Uchiyama, Adv. Mater. 18 (2006) 3318–3320.
[25] L. Bi, E. Fabbri, Z.Q. Sun, E. Traversa, Energy Environ. Sci. 4 (2011) 409–412.
[26] L. Malavasi, C.A.J. Fisher, M.S. Islam, Chem. Soc. Rev. 39 (2010) 4370–4387.
[27] T. Norby, Solid State Ionics 125 (1999) 1–11.
[28] Y. Yamazaki, F. Blanc, Y. Okuyama, L. Buannic, J.C. Lucio-Vega, C.P. Grey, S.M. Haile, Nat. Mater. 12 (2013) 647–651.
[29] T. Hibino, A. Hashimoto, M. Suzuki, M. Sano, J. Electrochem. Soc. 149 (2002) A1503–A1508.
[30] Z. Khani, M. Taillades-Jacquin, G. Taillades, D.J. Jones, M. Marrony, J. Rozière, Chem. Mater. 22 (2010) 1119–1125.
[31] A. D'Epifanio, E. Fabbri, E. Di Bartolomeo, S. Licoccia, E. Traversa, Fuel Cells 8 (2008) 69–76.
[32] Y. Yamazaki, R. Hernandez-Sanchez, S.M. Haile, Chem. Mater. 21 (2009) 2755–2762.
[33] H. Matsumoto, Y. Kawasaki, N. Ito, M. Enoki, T. Ishihara, Electrochem. Solid State Lett. 10 (2007) B77–B80.
[34] R. Raza, H.Y. Qin, L.D. Fan, K. Takeda, M. Mizuhata, B. Zhu, J. Power Sources 201 (2012) 121–127.
[35] E. Fabbri, D. Pergolesi, E. Traversa, Chem. Soc. Rev. 39 (2010) 4355–4369.
[36] B. Zhu, X.R. Liu, P. Zhou, X.T. Yang, Z.G. Zhu, W. Zhu, Electrochem. Commun. 3 (2001) 566–571.
[37] J.H. Tong, A. Subramaniyan, H. Guthrey, D. Clark, B.P. Gorman, R. O'Hayre, Solid State Ionics 211 (2012) 26–33.
[38] Y. Nishihata, J. Mizuki, T. Akao, H. Tanaka, M. Uenishi, M. Kimura, T. Okamoto, N. Hamada, Nature 418 (2002) 164–167.
[39] I. Hamada, A. Uozumi, Y. Morikawa, A. Yanase, H. Katayama-Yoshida, J. Am. Chem. Soc. 133 (2011) 18506–18509.
[40] D.M. Bierschenk, E. Potter-Nelson, C. Hoel, Y.G. Liao, L. Marks, K.R. Poeppelmeier, S.A. Barnett, J. Power Sources 196 (2011) 3089–3094.
[41] M.B. Katz, G.W. Graham, Y.W. Duan, H. Liu, C. Adamo, D.G. Schlom, X.Q. Pan, J. Am. Chem. Soc. 133 (2011) 18090–18093.
[42] J. Li, U.G. Singh, J.W. Bennett, K. Page, J.C. Weaver, J.P. Zhang, T. Proffen, A.M. Rappe, S. Scott, R. Seshadri, Chem. Mater. 19 (2007) 1418–1426.
[43] K.S. Knight, M. Soar, N. Bonanos, J. Mater. Chem. 7 (1992) 709–712.
[44] M.T. Caldes, K.V. Kravchyk, M. Benamira, N. Besnard, V. Gunes, O. Bohnke, O. Joubert, Chem. Mater. 24 (2012) 4641–4646.
[45] T. Pillo, R. Zimmermann, P. Steiner, S. Hüfner, J. Phys. Condens. Matter. 9 (1997) 3987–3999.
[46] K.R. Priolkar, P. Bera, P.R. Sarode, M.S. Hegde, S. Emura, R. Kumashiro, N.P. Lalla, Chem. Mater. 14 (2002) 2120–2128.
[47] P.J. Schmitz, K. Otto, J.E. de Vries, Appl. Catal. A 92 (1992) 59–72.
[48] K. Otto, L.P. Haack, J.E. de Vries, Appl. Catal. B 1 (1992) 1–12.
[49] U.G. Singh, J. Li, J.W. Bennett, A.M. Rappe, R. Seshadri, S.L. Scott, J. Catal. 249 (2007) 349–358.
[50] Y.M. Guo, Y. Lin, R. Ran, Z.P. Shao, J. Power Sources 193 (2009) 400–407.
[51] W. Grochala, P.P. Edwards, Chem. Rev. 104 (2004) 1283–1316.